

Effects of coil structure and electromagnetic shielding on plasma distribution and uniformity in large-area radio-frequency inductively coupled plasmas

Cheng Xin(辛程), Xiang-Yun Lyu(吕翔云), Si-Yu Xing(邢思雨), Yu-Ru Zhang(张钰如), Tao Liu(刘涛), Wei-Ping Le(乐卫平), Fei Gao(高飞), and You-Nian Wang(王友年)

Citation: Chin. Phys. B, 2026, 35 (**2**): 025201. DOI: 10.1088/1674-1056/ae2113
http://cpb.iphy.ac.cn; http://iopscience.iop.org/cpb

What follows is a list of articles you may be interested in

Experimental studies of H_2/Ar plasma in a cylindrical inductive discharge with an expansion region

Shi-Bo Li(李世博), Si-Yu Xing(邢思雨), Fei Gao(高飞), and You-Nian Wang(王友年)
Chin. Phys. B, 2024, 33 (**10**): 105201. DOI: 10.1088/1674-1056/ad6250

Electron characteristics and dynamics in sub-millimeter pulsed atmospheric dielectric barrier discharge

Junlin Fang(方骏林), Yarong Zhang(张亚容), Chenzi Lu(卢陈梓), Lili Gu(顾莉莉), Shaofeng Xu(徐少锋), Ying Guo(郭颖), and Jianjun Shi(石建军)
Chin. Phys. B, 2024, 33 (**1**): 015201. DOI: 10.1088/1674-1056/ad0118

Compared discharge characteristics and film modifications of atmospheric pressure plasma jets with two different electrode geometries

Xiong Chen(陈雄), Xing-Quan Wang(王兴权), Bin-Xiang Zhang(张彬祥), Ming Yuan(袁明), and Si-Ze Yang(杨思泽)
Chin. Phys. B, 2023, 32 (**11**): 115201. DOI: 10.1088/1674-1056/ace768

Numerical investigation of radio-frequency negative hydrogen ion sources by a three-dimensional fluid model

Ying-Jie Wang(王英杰), Jia-Wei Huang(黄佳伟), Quan-Zhi Zhang(张权治), Yu-Ru Zhang(张钰如), Fei Gao(高飞), and You-Nian Wang(王友年)
Chin. Phys. B, 2021, 30 (**9**): 095205. DOI: 10.1088/1674-1056/ac0e21

Discharge characteristic of very high frequency capacitively coupled argon plasma

Gui-Qin Yin(殷桂琴), Jing-Jing Wang(王兢婧), Shan-Shan Gao(高闪闪), Yong-Bo Jiang(姜永博), and Qiang-Hua Yuan(袁强华)
Chin. Phys. B, 2021, 30 (**9**): 095204. DOI: 10.1088/1674-1056/abf104

RAPID COMMUNICATION

Effects of coil structure and electromagnetic shielding on plasma distribution and uniformity in large-area radio-frequency inductively coupled plasmas

Cheng Xin(辛程)[1], Xiang-Yun Lyu(吕翔云)[1,†], Si-Yu Xing(邢思雨)[1], Yu-Ru Zhang(张钰如)[1], Tao Liu(刘涛)[2], Wei-Ping Le(乐卫平)[2], Fei Gao(高飞)[3,1,‡], and You-Nian Wang(王友年)[1]

[1] *Key Laboratory of Materials Modification by Laser, Ion, and Electron Beams (Ministry of Education), School of Physics, Dalian University of Technology, Dalian* 116024, *China*

[2] *Shenzhen CSL Vacuum Science and Technology Co., Ltd., Shenzhen* 518101, *China*

[3] *School of Integrated Circuits, Dalian University of Technology, Dalian* 116024, *China*

(Received 12 September 2025; revised manuscript received 2 November 2025; accepted manuscript online 19 November 2025)

Improving plasma uniformity is a critical issue in the development of large-area radio-frequency (RF) inductively coupled plasma (ICP) sources. In this work, the effects of coil structure and electromagnetic shielding on the spatial distribution and uniformity of the plasma are systematically investigated using a three-dimensional fluid model. The model integrates plasma and electromagnetic field modules to simulate the discharge characteristics of a large-area RF ICP source with dimensions of 100 cm × 50 cm. The results reveal that the electron density distribution varies significantly with the coil structure. For the rotating and translating coil structures, the electron density is high at off-axis positions and low at the center. In contrast, the mirror coil structure exhibits a significantly higher electron density at the chamber center, resulting in a high-center and low-edge density distribution. Among the three configurations, the rotating coil structure provides the best plasma uniformity. The incorporation of electromagnetic shielding further improves plasma uniformity, particularly for the mirror coil structure. For the rotating and translating coil structures, the electron density exhibits a saddle-shaped distribution regardless of electromagnetic shielding. However, introducing electromagnetic shielding into the mirror coil structure reduces the electron density at the chamber center and decreases the non-uniformity degree by 18.4%. Overall, the mirror coil structure with electromagnetic shielding achieves the highest uniformity, with an exceptional plasma uniformity of 94%. This work offers valuable insights for the design of large-area ICP sources in advanced plasma processing systems.

Keywords: large-area radio-frequency inductively coupled plasma, three-dimensional fluid model, plasma uniformity

PACS: 52.25.–b, 52.25.Fi, 52.65.–y, 52.80.Pi

DOI: 10.1088/1674-1056/ae2113 **CSTR:** 32038.14.CPB.ae2113

1. Introduction

Large-area inductively coupled plasma (ICP) sources are widely used for plasma etching, thin film deposition, material surface modification, and plasma cleaning in the semiconductor manufacturing and flat panel display industries due to their ability to generate high-density plasma under low-pressure conditions and to independently control plasma flux and ion energy.[1–10] However, the increasing dimensions of ICP sources have amplified the challenges associated with electromagnetic effects in inductively coupled discharges, including the skin effect, the standing wave effect, and the edge effect.[11] These challenges impede the generation of uniform plasma across large areas, adversely affecting the efficiency of etching and deposition processes and ultimately degrading product quality. Therefore, improving plasma uniformity in ICP sources is of paramount importance.

In recent years, researchers have proposed various strategies to improve plasma uniformity in ICP sources. One prominent approach involves optimizing coil and chamber structures.[12–18] Zhao *et al.*[12] developed a two dimensional (2D) self-consistent fluid model for a radio-frequency (RF) ICP source and demonstrated that adjusting the radial spacing of the coils enhanced plasma uniformity to 96%, while the chamber aspect ratio had a negligible influence. Kim *et al.*[13] utilized a passive resonant coil, which is a coil device that does not require an external power supply and achieves energy transfer through inductor–capacitor (LC) resonance and magnetic resonance coupling, to control the local electron and ion density distributions using experimental diagnostics in an inductively coupled argon gas discharge. The results revealed that the current flowing through the passive resonant coils reached a maximum value under resonant conditions, and the radial distributions of electron and ion densities became nearly flat. Lim *et al.*[14] investigated the effect of RF power

†Corresponding author. E-mail: xylv@dlut.edu.cn

‡Corresponding author. E-mail: fgao@dlut.edu.cn

© 2026 Chinese Physical Society and IOP Publishing Ltd. All rights, including for text and data mining, AI training, and similar technologies, are reserved.

applied to an internal linear-type antenna on plasma homogeneity in an ultra-large ICP source. They found that increasing the RF power improved plasma uniformity by increasing the plasma density near the chamber wall. Other studies have shown that gradient coil devices, chamber aspect ratios, Ni–Zn ferromagnetic-enhanced antennas (an improved antenna design that installs Ni–Zn ferrite material near a U-shaped inductively coupled plasma antenna; this material has high resistivity, high magnetic permeability, and excellent high-frequency characteristics, enabling it to concentrate and enhance the antenna's magnetic field), and parallel resonance coils (antenna structures that [18] reduce inductance by connecting coils in parallel, thereby lowering antenna voltage, and that use an external coil connected in series with a variable capacitor to induce LC resonance and regulate current distribution) could also modulate plasma uniformity.[15–17]

The application of external magnetic fields is another effective method for enhancing plasma uniformity.[19–21] Lee *et al.*[19] designed a magnetized ICP system in which the magnetic flux density increased radially and axially from the substrate center and found that flute instability (a macroscopic interchange instability caused by magnetic field gradients and plasma density gradients oriented in the same direction in magnetized plasmas, manifested as low-frequency slot-shaped disturbances) could be suppressed, resulting in increased plasma density and a significant reduction in nonuniformity. O'Connell *et al.*[20] demonstrated that a weak magnetic field gradient significantly improved plasma uniformity without scanning the position of the magnetic neutral loop, which is a three-dimensional ring structure with zero magnetic field strength produced by the bending of a quadrupole magnetic field in a specific coil configuration. Kim *et al.*[21] adopted multipolar magnetic fields in a large-area internal linear ICP source, which not only increased plasma density but also improved homogeneity by minimizing plasma diffusion toward the chamber edges. Additionally, RF bias has emerged as a viable technique for modulating plasma uniformity.[22–24] Huang *et al.*[22] employed a 2D hybrid model to investigate the influence of bias effects on stochastic heating and plasma uniformity in low-pressure ICP discharges. Their results indicated that higher bias amplitudes yielded a more uniform radial plasma distribution. This behavior arises because, under high bias voltage, pronounced stochastic sheath heating in the main chamber slows the reduction of electron density, while in the diffusion chamber, the discharge process is enhanced by stochastic sheath heating at both the substrate and the grounded metal chamber walls. The combined effect of these mechanisms leads to a more uniform plasma distribution. He *et al.*[23] connected an impedance control unit to the bias electrode to achieve series resonance in the ICP source, resulting in more uniform distributions of plasma potential, ion energy loss, and photoresist etch rates. Based on spatially resolved radial electron energy distribution function (EEDF) measurements, Lee *et al.*[24] observed that increasing RF bias power under high-pressure conditions significantly enhanced plasma uniformity, primarily due to relatively small ion losses near the radial edge and enhanced power deposition at the radial edge through the edge and skin effects.

Despite numerous studies on the uniformity of ICP sources, several problems remain unresolved. On the one hand, most simulation studies rely on 2D fluid or hybrid models, which inherently assume complete geometric symmetry and neglect many three-dimensional effects. These effects are critical to the discharge characteristics of ICP sources and the spatial distribution of plasma parameters. On the other hand, existing studies predominantly focus on chambers with dimensions limited to a few tens of centimeters, which simplifies the achievement of dense and uniform plasma. In large-area ICP discharges, however, the coil length becomes comparable to the electromagnetic wavelength, leading to standing wave effects associated with long coils,[25] which severely disrupt plasma uniformity.

To address the above issues, this study develops a three dimensional (3D) fluid model using COMSOL Multiphysics to investigate the effects of coil structure and electromagnetic shielding on the spatial distribution and uniformity of plasma in a large-area rectangular RF ICP source (dimensions: 100 cm × 50 cm). The paper is organized as follows. Section 2 provides a detailed description of the discharge chamber, coil structures, and the 3D fluid model, and presents model validation. Section 3 presents and discusses the results, focusing on the effects of coil structure and electromagnetic shielding on plasma distribution and uniformity. Finally, Section 4 summarizes the findings and proposes future research directions.

2. Model description

2.1. Discharge chamber and coil structure

The discharge chamber structure of the large-area rectangular RF ICP source is depicted in Fig. 1. The plasma region measures 100 cm in length, 50 cm in width, and 20 cm in height. The copper coils are positioned 1 cm above the dielectric window, which is composed of quartz with a thickness of 2 cm. The coils are surrounded by a 10 cm-high shield. The coordinate origin is defined at the center of the chamber bottom surface. The z-axis origin is located at this point, with the positive direction pointing from the bottom surface toward the top of the chamber. Argon is used as the discharge gas, and the RF power supply operates at a frequency of 13.56 MHz.

The dual-coil configuration includes three types of coil structures: rotating coil, translating coil, and mirror coil, as shown in Fig. 2. In the rotating coil structure (see Fig. 2(a)),

each coil comprises four turns, with a spacing of 4 cm between adjacent turns. The distance between the outermost coil and the chamber wall is also 4 cm, and the coil cross section has a radius of 0.5 cm. The right coil is obtained by rotating the left coil by 180° around the z-axis. The translating coil structure (see Fig. 2(b)) is constructed by shifting the left coil 48 cm to the right while preserving identical dimensions for both coils. The mirror coil structure (see Fig. 2(c)) is characterized by a mirror-symmetrical arrangement of the left and right coils with respect to the chamber center. In all studied coil structures, the currents are supplied from the outer sides of the coils.

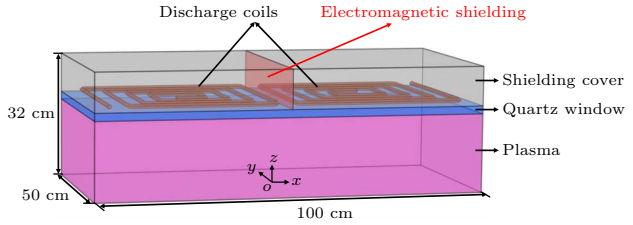


Fig. 1. Schematic diagram of the large-area rectangular RF ICP source.

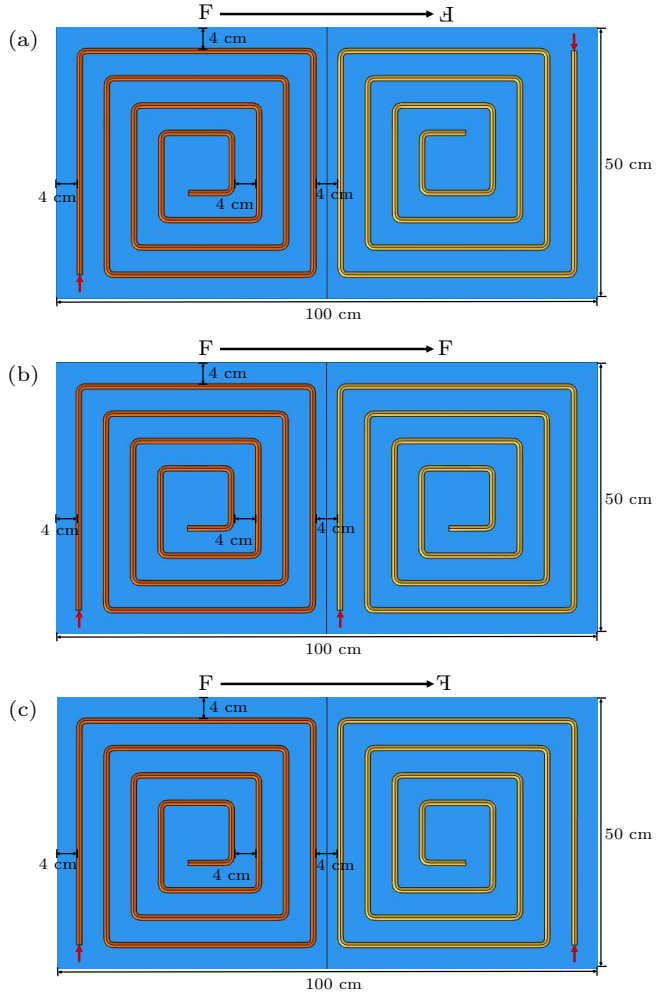


Fig. 2. Schematic of the dual-coil configuration: (a) rotating coil structure, (b) translating coil structure, and (c) mirror coil structure.

2.2. Three-dimensional fluid model

We utilized COMSOL to construct a three-dimensional large-area ICP source geometry model including three coil structures and an electromagnetic shielding device. A self-defined mesh division scheme was adopted to achieve a balance between computational accuracy and efficiency. Under appropriate initial and boundary conditions, the 3D fluid model, integrated with both the plasma and electromagnetic field modules, was coupled to the large-area ICP source for self-consistent calculations, thereby obtaining the spatial distribution of plasma parameters. All equations involved in the model adhere to the official COMSOL technical documentation.[26]

2.2.1. Plasma module

The plasma module includes the fluid equations for electrons and heavy particles. The electron continuity equation is expressed as

$$\frac{\partial n_{\mathrm{e}}}{\partial t}+\nabla\cdot\boldsymbol{\Gamma}_{\mathrm{e}}=R_{\mathrm{e}}, \tag{1}$$

where n_{e} and $\boldsymbol{\Gamma}_{\mathrm{e}}$ represent the electron density and flux, respectively, and R_{e} is the source term. $\boldsymbol{\Gamma}_{\mathrm{e}}$ is derived using the drift-diffusion approximation

$$\boldsymbol{\Gamma}_{\mathrm{e}}=-\left(\mu_{\mathrm{e}}\cdot\boldsymbol{E}\right)n_{\mathrm{e}}-D_{\mathrm{e}}\cdot\nabla n_{\mathrm{e}}, \tag{2}$$

where μ_{e} and D_{e} are the mobility and diffusion coefficients of electrons, respectively, and $\boldsymbol{E}$ represents the electrostatic field. In Eq. (2), the first term on the right-hand side represents the electron drift flux induced by the electrostatic field, and the second term represents the electron diffusion flux induced by the density gradient. R_{e} accounts for electron generation and loss, and is defined as

$$R_{\mathrm{e}}=\sum_{j}k_j n_a n_b, \tag{3}$$

where n_a and n_b are the reactant number densities and k_j is the rate coefficient for reaction j, which can be calculated from the cross-section data as follows:

$$k_j=\gamma\int_0^{\infty}\varepsilon\sigma_j(\varepsilon)f(\varepsilon)\,\mathrm{d}\varepsilon, \tag{4}$$

where $\gamma=\sqrt{2q/m_{\mathrm{e}}}$ is a coefficient, q is the electron charge, and m_{e} is the electron mass. ε denotes the electron energy, σ_j is the collision cross section, and f is the electron energy distribution function.

Additionally, the electron energy satisfies the following energy conservation equation:

$$\frac{\partial n_\varepsilon}{\partial t}+\nabla\cdot\boldsymbol{\Gamma}_\varepsilon+\boldsymbol{E}\cdot\boldsymbol{\Gamma}_{\mathrm{e}}=R_\varepsilon+P_{\mathrm{ind}}, \tag{5}$$

where n_ε and $\boldsymbol{\Gamma}_\varepsilon$ are the electron energy density and flux, respectively, R_ε represents the energy loss or gain resulting from

inelastic collisions, and P_{ind} is the inductive power deposition density. $\boldsymbol{\Gamma}_\varepsilon$ is expressed as

$$\boldsymbol{\Gamma}_\varepsilon = -(\mu_\varepsilon \cdot \boldsymbol{E})\, n_\varepsilon - D_\varepsilon \cdot \nabla n_\varepsilon, \tag{6}$$

where μ_ε and D_ε are the mobility and diffusion coefficients of electron energy. The electron energy density is calculated as $n_\varepsilon = 3n_{\mathrm{e}}T_{\mathrm{e}}/2$, where T_{e} represents the electron temperature. The source term for the electron energy is obtained by summing the non-collisional energy loss or gain over all reactions

$$R_\varepsilon = \sum_j k_j n_a n_b \varepsilon_j, \tag{7}$$

where ε_j is the threshold energy for reaction j. In this way, the electron density and energy distributions can be obtained by solving the above equations.

In addition to electron dynamics, this module incorporates the transport processes of heavy species, including ions and neutral particles, which are described by the following multicomponent equations:

$$\rho \frac{\partial w_k}{\partial t} = \nabla \cdot \boldsymbol{j}_k + R_k, \tag{8}$$

$$\boldsymbol{j}_k = \rho w_k \boldsymbol{V}_k, \tag{9}$$

$$\boldsymbol{V}_k = D_k \nabla \ln w_k + D_k \nabla \ln M_{\mathrm{n}} - q_k \mu_k \boldsymbol{E}, \tag{10}$$

where w_k, $\boldsymbol{j}_k$, and $\boldsymbol{V}_k$ are the mass fraction, diffusion flux vector, and multicomponent diffusion velocity of heavy species k, respectively, and R_k is the source term. $\rho = M_{\mathrm{n}}P_{\mathrm{A}}/(RT)$ is the mixture density, where M_{n} is the average molar mass, P_{A} is the pressure, R is the universal gas constant, and T is the gas temperature. In Eq. (10), D_k and μ_k are the diffusion coefficient and mobility of species k, respectively, and q_k is the particle charge. For neutral particles, the last term in Eq. (10) can be neglected. The diffusion coefficient for ions and neutral particles is expressed as

$$D_k = \frac{1 - w_k}{\sum_{j \neq k} x_j / D_{kj}}, \tag{11}$$

where D_{kj} is the binary diffusion coefficient between species k and j, and x_j is the mole fraction of species j. The ion mobility is calculated from the ion diffusion coefficient using the Einstein relation ($D_k/\mu_k = T_k/e$).

2.2.2. Electromagnetic field module

The electromagnetic field is described by Maxwell's equations, which are given as follows:

$$\left(\mathrm{j}\omega\sigma_{\mathrm{p}} - \omega^2 \varepsilon_0 \varepsilon_{\mathrm{r}}\right) \boldsymbol{A} + \nabla \times \left(\mu_0^{-1}\mu_{\mathrm{r}}^{-1}\boldsymbol{B}\right) = \boldsymbol{J}_{\mathrm{coil}}, \tag{12}$$

$$\boldsymbol{B} = \nabla \times \boldsymbol{A}, \tag{13}$$

where j is the imaginary unit, ω is the angular frequency of the power source, and σ_{p} is the plasma conductivity. ε_0 and ε_{r} are the vacuum permittivity and the relative permittivity of the material, respectively. ε_{r} is set to 1 for the vacuum and plasma regions and to 4.2 for the quartz window. Similarly, μ_0 and μ_{r} are the vacuum magnetic permeability and the relative magnetic permeability of the medium, with μ_{r} set to 1 in this model. $\boldsymbol{A}$ is the magnetic vector potential, $\boldsymbol{B}$ is the magnetic field, and $\boldsymbol{J}_{\mathrm{coil}}$ is the coil current density.

In addition, the inductive power deposition density is calculated as

$$P_{\mathrm{ind}} = \frac{1}{2}\mathrm{Re}\left(\boldsymbol{E}_{\mathrm{ind}}^* \cdot \boldsymbol{J}_{\mathrm{p}}\right), \tag{14}$$

where $\boldsymbol{E}_{\mathrm{ind}} = \mathrm{j}\omega\boldsymbol{A}$ is the inductive electric field, and $\boldsymbol{E}_{\mathrm{ind}}^*$ denotes its complex conjugate. According to Ohm's law, the plasma current density is given by $\boldsymbol{J}_{\mathrm{p}} = \sigma_{\mathrm{p}} \cdot \boldsymbol{E}_{\mathrm{ind}}$.

The plasma potential and the electrostatic field are obtained by solving the Poisson equation, as shown below:

$$\nabla \cdot \boldsymbol{D} = \rho_V, \tag{15}$$

$$\boldsymbol{E} = -\nabla V, \tag{16}$$

where ρ_V represents the space charge density, which is automatically computed based on the plasma chemistry defined in the model. $\boldsymbol{D} = \varepsilon_0\varepsilon_{\mathrm{r}}\boldsymbol{E}$ is the electric displacement vector, and V is the plasma potential.

2.2.3. Boundary conditions

Since the drift effect, secondary electron emission, and thermal emission are neglected in this model, the boundary conditions for the electron flux and electron energy flux are defined as

$$\boldsymbol{n} \cdot \boldsymbol{\Gamma}_{\mathrm{e}} = \frac{1 - r_{\mathrm{e}}}{1 + r_{\mathrm{e}}}\left(\frac{1}{2}v_{\mathrm{e,th}}n_{\mathrm{e}}\right), \tag{17}$$

$$\boldsymbol{n} \cdot \boldsymbol{\Gamma}_\varepsilon = \frac{1 - r_{\mathrm{e}}}{1 + r_{\mathrm{e}}}\left(\frac{5}{6}v_{\mathrm{e,th}}n_{\mathrm{e}}\right), \tag{18}$$

where $\boldsymbol{n}$ is the outward normal vector, r_{e} is the reflection coefficient, and $v_{\mathrm{e,th}} = \sqrt{8T_{\mathrm{e}}/(\pi m_{\mathrm{e}})}$ is the thermal velocity of electrons. As neutral particles and ions are generally lost at the chamber walls, the inward mass flux is expressed as

$$\boldsymbol{n} \cdot \boldsymbol{\Gamma}_k = M_k R_k + M_k c_k q_k \mu_k (\boldsymbol{E} \cdot \boldsymbol{n}), \tag{19}$$

where M_k and c_k are the molar mass and molar concentration of species k, respectively. For neutral particles, only the first term is considered.

In the electromagnetic field module, a magnetically insulating boundary condition is applied to all outer walls of the discharge chamber

$$\boldsymbol{n} \times \boldsymbol{A} = 0. \tag{20}$$

Additionally, the bottom and side walls of the plasma region are grounded, leading to the following boundary condition for the plasma potential:

$$V = 0. \tag{21}$$

2.2.4. Initial conditions and mesh configuration

For convenience in the calculations, the model also defines several initial conditions, including an initial electron density of 1×10^{16} m^{-3}, an initial average electron energy of 4 eV, an initial gas temperature of 300 K, and an initial plasma potential of 0 V.

The numerical framework is based on the finite element method, which allows the use of triangular mesh grids at boundaries and tetrahedral grids in the volume. The coil structures employ swept meshes; the interface between the plasma region and the quartz window uses extremely refined free triangular meshes; the plasma region uses extremely refined free tetrahedral meshes, with additional boundary layer meshes applied to refine the plasma region boundaries; the remaining regions use relatively refined free tetrahedral meshes. The complete mesh comprises 1064703 domain elements, 55452 boundary elements, and 8896 edge elements.

2.2.5. Ar plasma reactions

The model includes four species (e, Ar, Ar^+, Ars) and nine reactions. The expressions, reaction types, and threshold energies of these reactions are listed in Table 1.

Table 1. Reactions for Ar plasma.

No.	Reaction	Type	$\Delta\varepsilon$ (eV)	Reference
1	$e + Ar \rightarrow e + Ar$	elastic	0	[27]
2	$e + Ar \rightarrow e + Ars$	excitation	11.5	[27]
3	$e + Ars \rightarrow e + Ar$	super-elastic	−11.5	[27]
4	$e + Ar \rightarrow 2e + Ar^+$	ionization	15.8	[27]
5	$e + Ars \rightarrow 2e + Ar^+$	ionization	4.427	[27]
6	$Ars + Ars \rightarrow e + Ar + Ar^+$	penning ionization	–	[28]
7	$Ars + Ar \rightarrow Ar + Ar$	metastable quenching	–	[28]
8	$Ars + wall \rightarrow Ar$	surface reaction	–	[29]
9	$Ar^+ + wall \rightarrow Ar$	surface reaction	–	[29]

2.3. Model validation

To ensure the reliability of the proposed model, simulations performed using the fluid model developed in this study are compared with experimental results reported in Ref. [30]. The cylindrical reactor has a height of 19 cm and a radius of 13 cm. An RF power of 13.56 MHz is applied to a two-turn planar antenna with an inner diameter of 18 cm and an outer diameter of 21 cm. The discharge conditions are maintained at an argon gas pressure of 50 mTorr and a power of 100 W. Figure 3 illustrates the radial profiles of ion density at different gap lengths, where the solid lines represent the experimental results and the dashed lines indicate the simulation results obtained using this model. The comparison reveals strong agreement between the experimental and simulated results, with both exhibiting consistent trends across the radial profiles. However, the ion density predicted by the simulations is slightly higher than that observed in the experimental measurements. This discrepancy arises from differences in power interpretation: the experimental power corresponds to the output power of the power supply, which includes matching losses and does not represent the actual power coupled to the plasma, whereas the simulations account for the power directly deposited into the plasma.[31] As a result, the simulated ion density is marginally higher than the experimental values, while the overall trend remains consistent, confirming the accuracy and validity of the model.

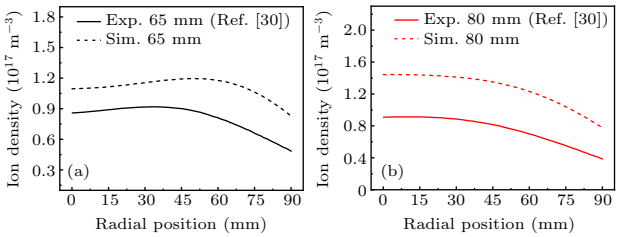


Fig. 3. Radial profiles of the ion density for different gap lengths at 100 W and 50 mTorr: (a) a gap length of 65 mm and (b) a gap length of 80 mm. The results are compared with the experimental data reported in Ref. [30].

To quantitatively validate the interpretation of this power discrepancy, we performed supplementary simulations under the same conditions. Figure 4 presents the radial distribution of argon ion density at different simulated powers for gap lengths of 65 mm and 80 mm. The figure reveals that as the simulated power decreases, the ion density correspondingly decreases, and the simulated results gradually approach the experimental results. For a gap length of 65 mm, the simulated curve at 80 W coincides with the experimental curve within the 0–45 mm range, while the simulated curve at 60 W coincides with the experimental curve within the 45–90 mm range. For a gap length of 80 mm, the simulated curve at 65 W coincides with the experimental curve within the 0–45 mm range, whereas the simulated curve at 50 W coincides with the experimental curve within the 45–90 mm range. These results confirm that the interpretation of power loss in the experiment is reasonable and further reinforce the reliability of the consistency analysis between the model and the experiment.

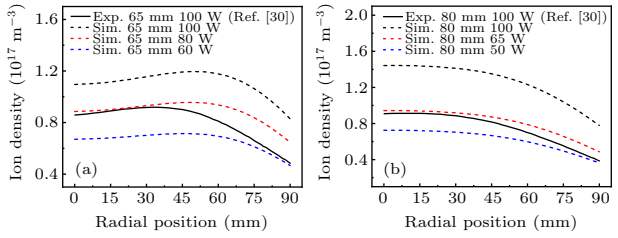


Fig. 4. Radial profiles of the ion density for different simulated powers at 50 mTorr: (a) a gap length of 65 mm and (b) a gap length of 80 mm. The results are compared with the experimental data reported in Ref. [30].

It should be noted that the reference experimental system used for model verification is a small cylindrical chamber, while the main subject of this study is a large-area rectangular ICP source. Although the core physical framework of the model is applicable across both scales, and the validation results confirm the model's accuracy in capturing fundamental physical mechanisms, differences in geometric symmetry

and dimensions between the two systems should be regarded as a potential limitation. The experimental setup for a large-area plasma source is currently under design and construction; however, the equipment development cycle is relatively long. Our simulations are intended to provide guidance for future experiments, which will be conducted in the next step of this study.

3. Results and discussion

3.1. Effect of coil structure on plasma distribution

This subsection investigates the effect of coil structure without electromagnetic shielding on the spatial distribution of plasma. The simulations are performed under the following discharge conditions: chamber height of 20 cm, RF power of 1000 W per coil, pressure of 5 Pa, and coil spacing of 4 cm. This study focuses on plasma distribution near the substrate surface, as it most directly impacts the uniformity of processes such as etching and deposition. The substrate stage is typically located at the bottom of the discharge chamber. Therefore, unless otherwise specified, the *xy*-plane distributions presented in this paper are taken from the cross-section near the chamber bottom ($z = 2$ cm), approximating the plane where the substrate is positioned.

Figure 5 presents the plasma parameter distributions in the *xy*-plane for different coil structures without electromagnetic shielding. The first, third, and fourth rows show the distributions of electron density, electron source term, and electron flux in the *xy*-plane ($z = 2$ cm), respectively, while the sixth row shows the distributions of electric field in the *xy*-plane ($z = 19.5$ cm). The electric field reported here is the vector sum of the three components E_x, E_y, and E_z. Data at $z = 19.5$ cm are shown because the inductive electric field generated by the coil rapidly decays upon entering the plasma due to the skin effect; the skin depth is much smaller than the chamber size. At the chamber bottom ($z = 2$ cm), the electric field has decayed to a weak level and lost its spatial distribution characteristics. All fluxes depicted in the figures represent projections of vector flux onto the corresponding plane, while the source term represents the volume source term. In Figs. 5(j)–5(r), the color bar indicates the magnitude of vector values, and the arrow length and direction represent vector magnitude and direction, respectively.

From Figs. 5(a)–5(c), it is evident that for the rotating and translating coil structures, the electron density is high at off-axis positions symmetrically located on both sides of the chamber center (approximately $x = \pm 25$ cm, corresponding to the 1/4 and 3/4 points of the chamber length) and low at the center. In contrast, the mirror coil structure exhibits high density at the center and low density at the edges. This behavior results from the interplay between electron generation (characterized by the source term) and transport (characterized by the electron flux) processes.[15,32] For the rotating and translating coil structures, the electron source term is notably higher at off-axis positions (see Figs. 5(g) and 5(h)). Furthermore, the electron flux (Figs. 5(j) and 5(k)) shows that electrons move towards the off-axis positions due to electric field migration and gradient diffusion, forming the observed density distribution. In the mirror coil structure, although the electron flux is directed towards the edges, the strong electric field at the center of the *xy*-plane leads to an extremely high electron source term (see Fig. 5(i)), resulting in high central electron density.

Among the coil configurations, the mirror coil structure exhibits a significantly higher electron density at the center of the *xy*-plane compared to the rotating and translating coil structures. This arises from differences in current directions within the coils: for the rotating and translating structures, currents at the *xy*-plane center flow in opposite directions, whereas the mirror coil structure maintains consistent current directions across both coils. This alignment enhances mutual inductance, concentrating currents near the center, generating a stronger magnetic field, inducing a stronger electric field, and producing higher electron density. An asymmetric electron density distribution (see Fig. 5(b)) is observed in the translating coil structure, likely because the coil is not fully enclosed, causing asymmetry in the coil opening relative to $x = 0$ cm. The current return path is inherently asymmetric with respect to chamber boundaries, producing a lower electron source term on one side and a higher electron source term on the other. The resulting electron density exhibits a low concentration on the left and a high concentration on the right.

The second and fifth rows of Fig. 5 show the distributions of electron temperature and electron energy flux in the *xy*-plane ($z = 2$ cm), respectively. While the maximum electron temperature remains similar across the three configurations, the mirror coil structure exhibits elevated electron temperature near $x = 0$ cm (see Fig. 5(f)). As shown in Figs. 5(m)–5(o), the mirror coil structure also facilitates higher electron energy flux compared with the rotating and translating coil structures, resulting in increased electron temperature in the central region.

Figure 6 illustrates the plasma parameter distributions in the *xz*-plane for different coil structures without electromagnetic shielding. The first, third, and fourth rows show the distributions of electron density, electron source term, and electron flux in the *xz*-plane ($y = 0$ cm), respectively. It can be observed that the mirror coil structure exhibits the highest electron density at the chamber center compared to the rotating and translating coil structures. This trend can be explained in terms of both generation and transport. On one hand, the central electric field is stronger in the mirror coil structure, resulting in a higher electron source term (see Fig. 6(i)). On the other hand, as illustrated in Figs. 6(j)–6(l), electrons in the ro-

tating and translating coil structures primarily move towards the chamber edges, thereby reducing the central electron density. In contrast, the mirror coil structure propels electrons vertically upwards near $x = 0$ cm, leading to a markedly increased electron density at the chamber center.

The second and fifth rows of Fig. 6 show the distributions of electron temperature and deposited power density in the xz-plane ($y = 0$ cm), respectively. The rotating and translating coil structures exhibit a bimodal temperature distribution near $x = 0$ cm, whereas the mirror coil structure generates a unimodal temperature distribution. This difference is primarily determined by the spatial distributions of deposited power density, as clearly shown in Figs. 6(m)–6(o). In this study, the power deposition distribution is dominated by the standard skin and edge effects, with no evidence of standing wave effects at all. This is because the ICP source operates at a frequency of 13.56 MHz, corresponding to a wavelength of approximately 22 m, while the total coil length is 4.27 m, which is far shorter than half of the electromagnetic wavelength. Therefore, no macroscopic resonant standing waves are generated, and the power deposition distribution exhibits no standing wave characteristics.

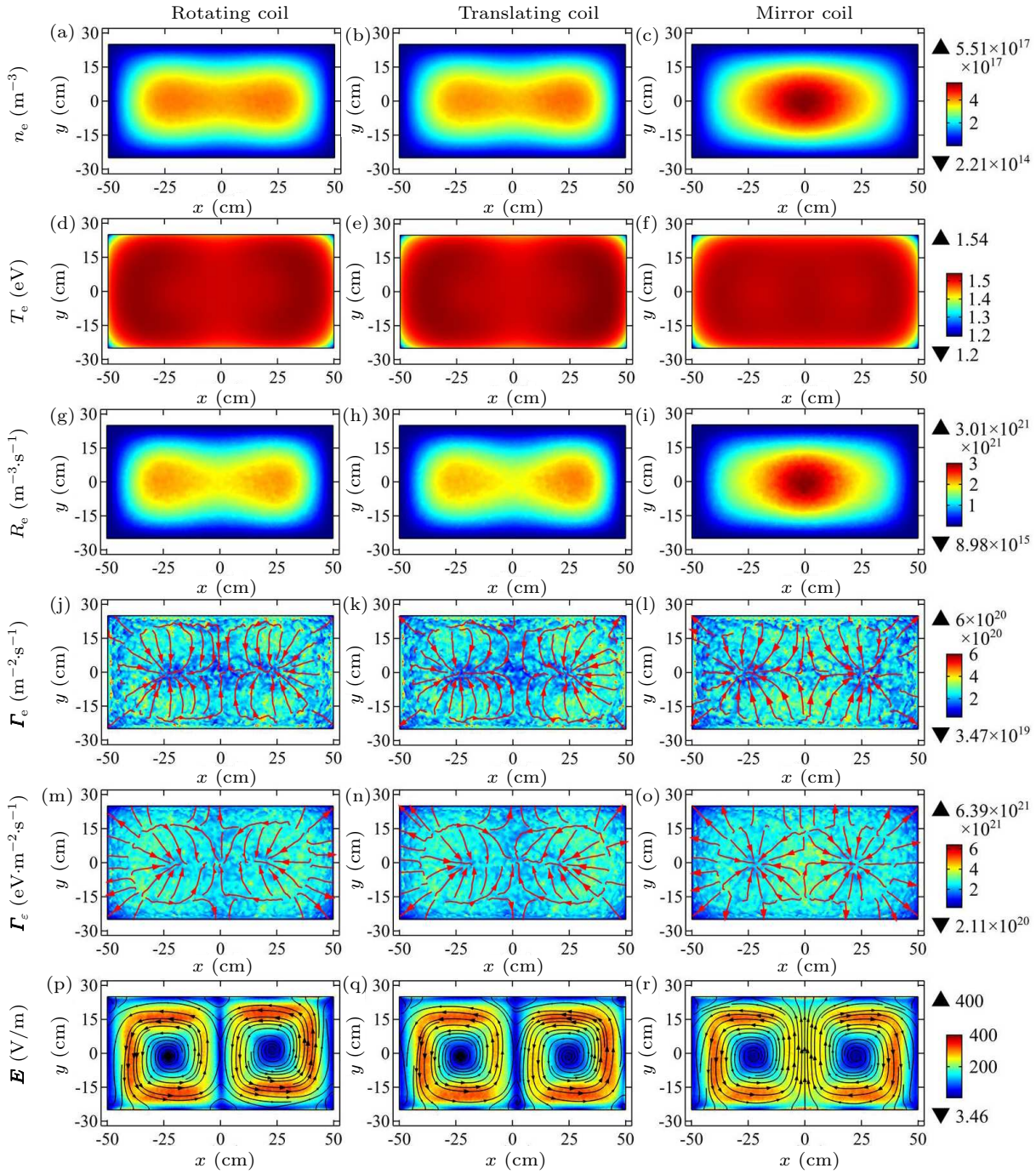


Fig. 5. Distributions of electron density (first row), electron temperature (second row), electron source term (third row), electron flux (fourth row), and electron energy flux (fifth row) in the xy-plane ($z = 2$ cm), as well as the electric field (sixth row) in the xy-plane ($z = 19.5$ cm), for different coil structures without electromagnetic shielding.

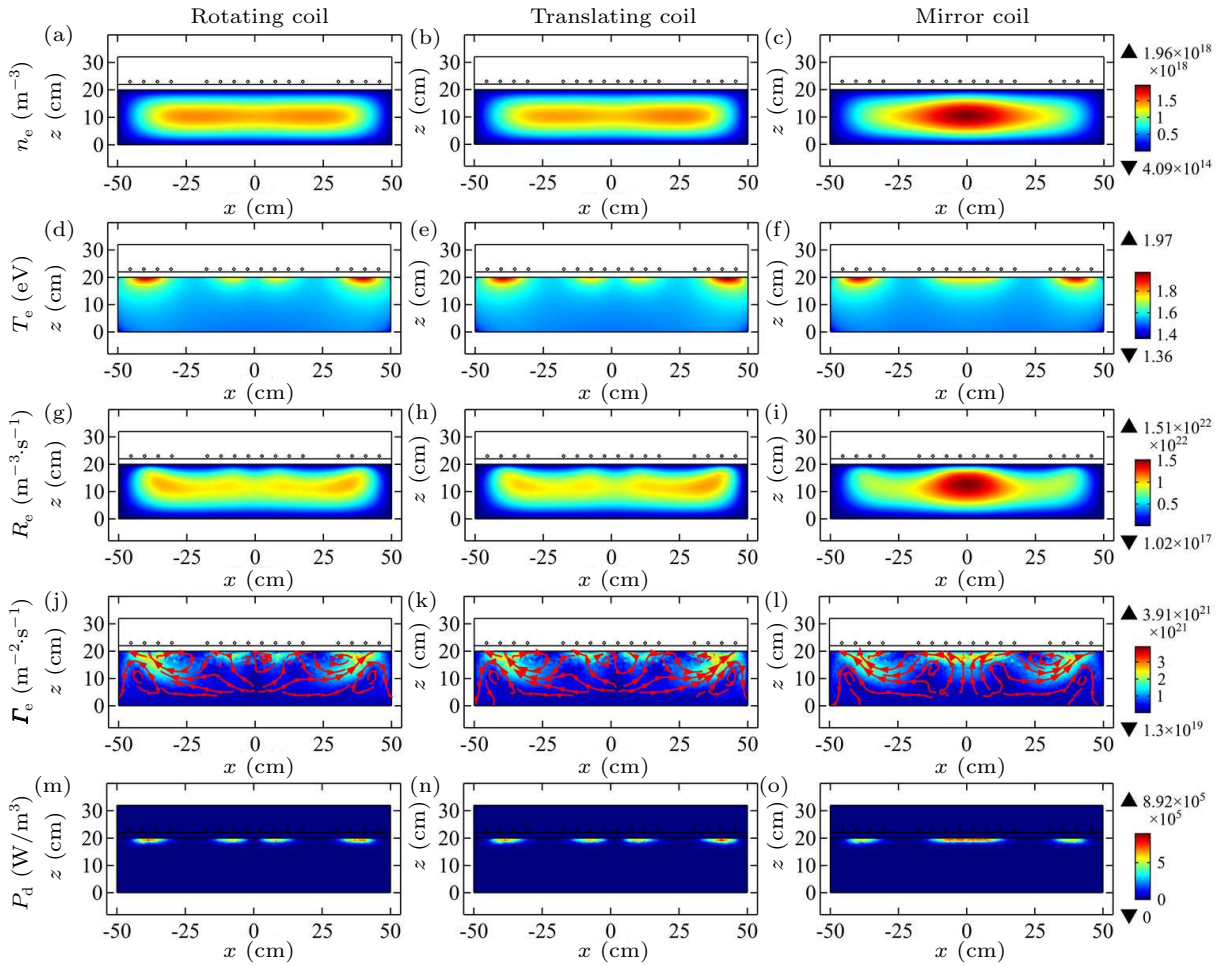


Fig. 6. Distributions of electron density (first row), electron temperature (second row), electron source term (third row), electron flux (fourth row), and deposited power density (fifth row) in the xz-plane ($y = 0$ cm) for different coil structures without electromagnetic shielding.

In RF ICP discharges, the inductive electric field generated by the coil decays rapidly upon entering the plasma, and the penetration depth of the electromagnetic field is much smaller than the chamber dimensions. Consequently, the deposited power is primarily concentrated near the upper surface of the plasma region. For the rotating and translating coil structures, the deposited power density peaks on either side of $x = 0$ cm, producing a bimodal temperature distribution. In contrast, the mirror coil structure consolidates these two peaks into a single central peak near $x = 0$ cm, resulting in a unimodal temperature distribution.

As an example of the mirror coil structure without electromagnetic shielding, we systematically analyzed the contributions of the dominant transport terms in distinct regions. The electron flux comprises a drift term driven by the electrostatic field and a diffusion term driven by the density gradient. To elucidate the dominant transport mechanisms in the central and edge regions, Figs. 7–9 present the distributions of electron flux, drift electron flux, and diffusion electron flux in the xy-plane along the x, y, and z directions, respectively, for the mirror coil structure without electromagnetic shielding. Similarly, Figs. 10–12 show the distributions of electron flux, drift electron flux, and diffusion electron flux in the xz-plane along the x, y, and z directions, respectively, for the same configuration.

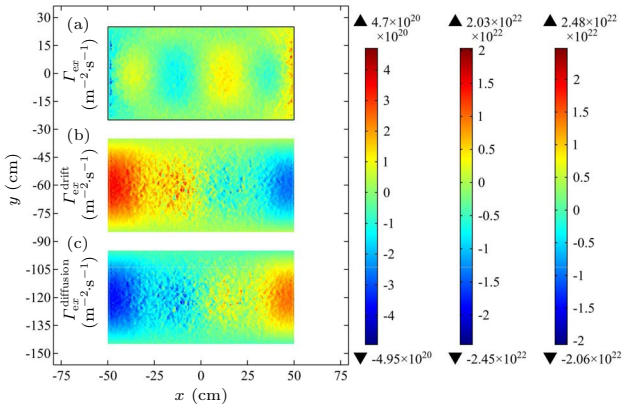


Fig. 7. Distributions of (a) electron flux, (b) drift electron flux, and (c) diffusion electron flux in the x-direction in the xy-plane ($z = 2$ cm) for the mirror coil structure without electromagnetic shielding.

As seen from the figures, the bipolar electric field confines electrons toward the chamber center, resulting in the drift electron flux pointing centrally. Meanwhile, the high electron density at the chamber center and the low electron density near the wall edges establish a density gradient between the center and edges, which drives the diffusion electron flux outward toward the chamber walls. Consequently, the transport process

in the central region is dominated by the drift electron flux, while in the wall edge region it is dominated by the diffusion electron flux. In the intermediate regions, the transport is influenced by both drift and diffusion electron fluxes.

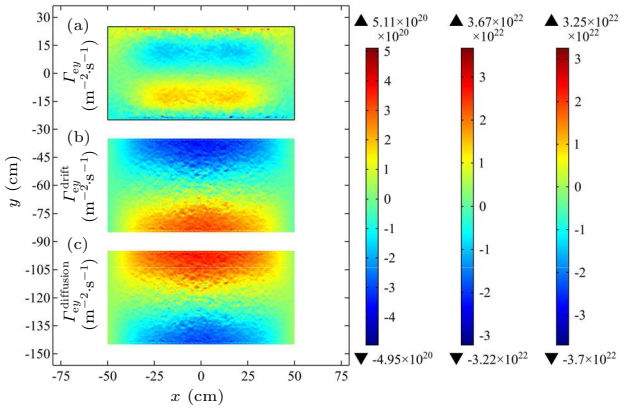


Fig. 8. Distributions of (a) electron flux, (b) drift electron flux, and (c) diffusion electron flux in the y-direction in the xy-plane ($z = 2$ cm) for the mirror coil structure without electromagnetic shielding.

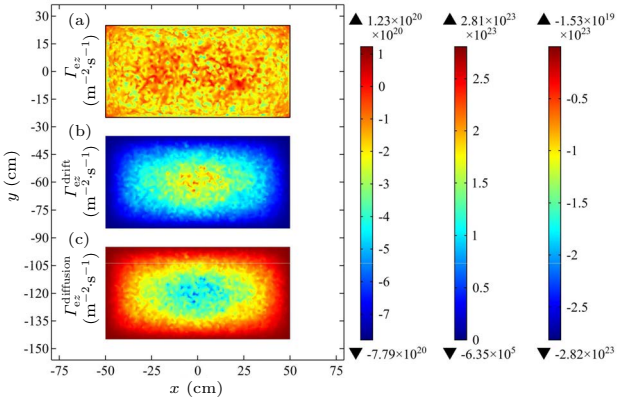


Fig. 9. Distributions of (a) electron flux, (b) drift electron flux, and (c) diffusion electron flux in the z-direction in the xy-plane ($z = 2$ cm) for the mirror coil structure without electromagnetic shielding.

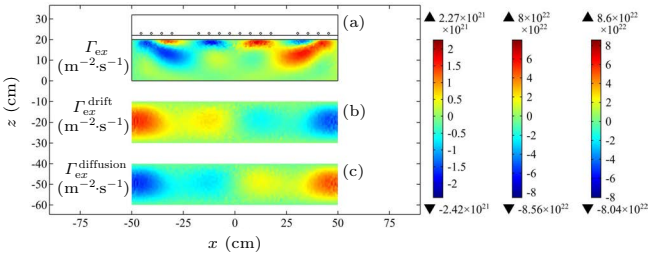


Fig. 10. Distributions of (a) electron flux, (b) drift electron flux, and (c) diffusion electron flux in the x-direction in the xz-plane ($y = 0$ cm) for the mirror coil structure without electromagnetic shielding.

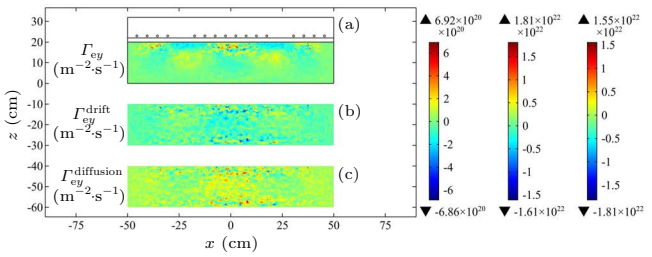


Fig. 11. Distributions of (a) electron flux, (b) drift electron flux, and (c) diffusion electron flux in the y-direction in the xz-plane ($y = 0$ cm) for the mirror coil structure without electromagnetic shielding.

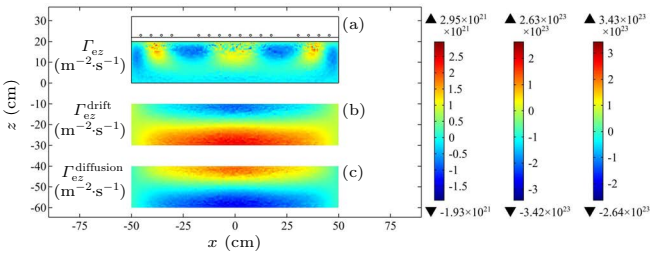


Fig. 12. Distributions of (a) electron flux, (b) drift electron flux, and (c) diffusion electron flux in the z-direction in the xz-plane ($y = 0$ cm) for the mirror coil structure without electromagnetic shielding.

3.2. Effect of electromagnetic shielding on plasma distribution

This subsection examines the influence of electromagnetic shielding on the spatial distribution of plasma. Electromagnetic shielding is implemented by placing a metal spacer between the two coils, which is numerically treated as a magnetic insulator via the boundary condition $\boldsymbol{n} \times \boldsymbol{A} = 0$. The discharge conditions described in the previous subsection are consistently maintained.

Figure 13 shows the plasma parameter distributions in the xy-plane for different coil structures with electromagnetic shielding. The first, third, and fourth rows present the distributions of electron density, electron source term, and electron flux in the xy-plane ($z = 2$ cm), respectively, while the sixth row presents the distributions of the electric field in the xy-plane ($z = 19.5$ cm). Comparing Figs. 5 and 13 reveals distinct shielding effects across the coil configurations.

For the rotating coil structure, electromagnetic shielding does not noticeably affect the spatial distribution of electron density. In the translating coil structure, shielding effectively eliminates the left-right asymmetry in electron density about the symmetry axis. This improvement results from the decoupling of coil interactions by the shielding, producing a symmetric electron source term (see Fig. 13(h)), and thus a symmetric electron density distribution around the center of the xy-plane.

In the mirror coil structure, incorporating electromagnetic shielding reduces the electron density at the center of the xy-plane. This reduction occurs because the shielding suppresses mutual inductance between the coils, thereby decreasing the electric field near $x = 0$ cm (see Fig. 13(r)). Consequently, the electron source term diminishes, leading to a lower electron density in the central region.

The second and fifth rows of Fig. 13 show the distributions of electron temperature and electron energy flux in the xy-plane ($z = 2$ cm), respectively. Electromagnetic shielding does not significantly influence the electron energy flux in the rotating and translating coil structures, resulting in negligible changes in the electron temperature distributions. However, for the mirror coil structure, shielding reduces the electron energy flux at the center of the xy-plane, leading to a lower electron temperature near $x = 0$ cm.

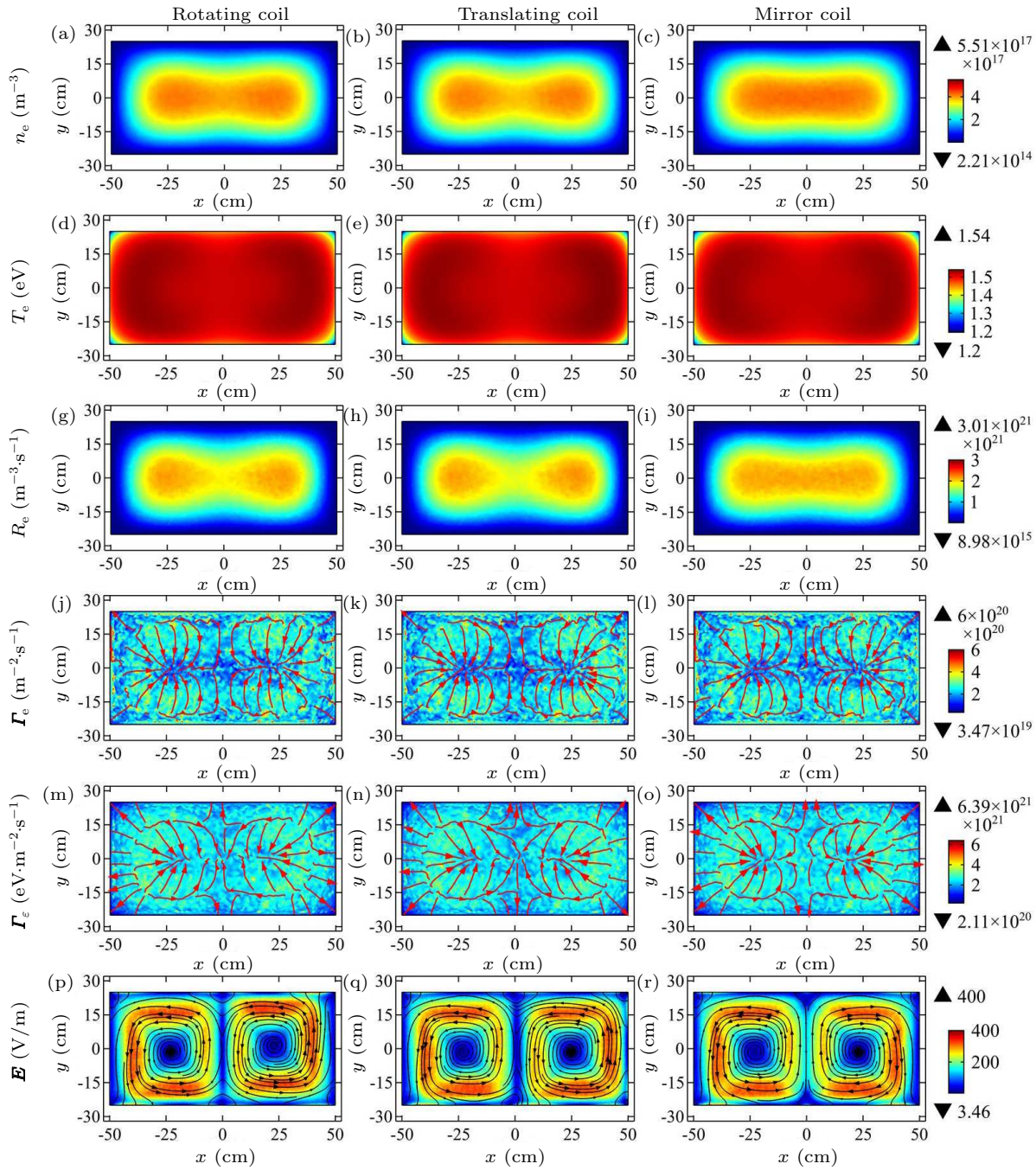


Fig. 13. Distributions of electron density (first row), electron temperature (second row), electron source term (third row), electron flux (fourth row), and electron energy flux (fifth row) in the xy-plane ($z = 2$ cm), as well as the electric field (sixth row) in the xy-plane ($z = 19.5$ cm), for different coil structures with electromagnetic shielding.

Figure 14 depicts the plasma parameter distributions in the xz-plane for different coil structures with electromagnetic shielding. The first, third, and fourth rows show the distributions of electron density, electron source term, and electron flux in the xz-plane ($y = 0$ cm), respectively. By comparing Figs. 6 and 14, the effect of electromagnetic shielding on different coil structures becomes evident.

For the rotating coil structure, electromagnetic shielding has a negligible influence on the electron density distribution. For the translating coil structure, shielding significantly enhances the symmetry of the electron density. In the mirror coil structure, introducing electromagnetic shielding reduces the electron density at the chamber center. This reduction arises from two factors: First, the shielding weakens the central electric field, resulting in a decreased electron source term (see Fig. 14(i)). Second, as shown in Fig. 14(l), electrons in the central region exhibit both upward motion and lateral diffusion toward the chamber edges under shielding. These combined effects lead to a reduced electron density at the chamber center.

The second and fifth rows of Fig. 14 show the distributions of electron temperature and deposited power density in the xz-plane ($y = 0$ cm), respectively. For the rotating and translating coil structures, the electron temperature

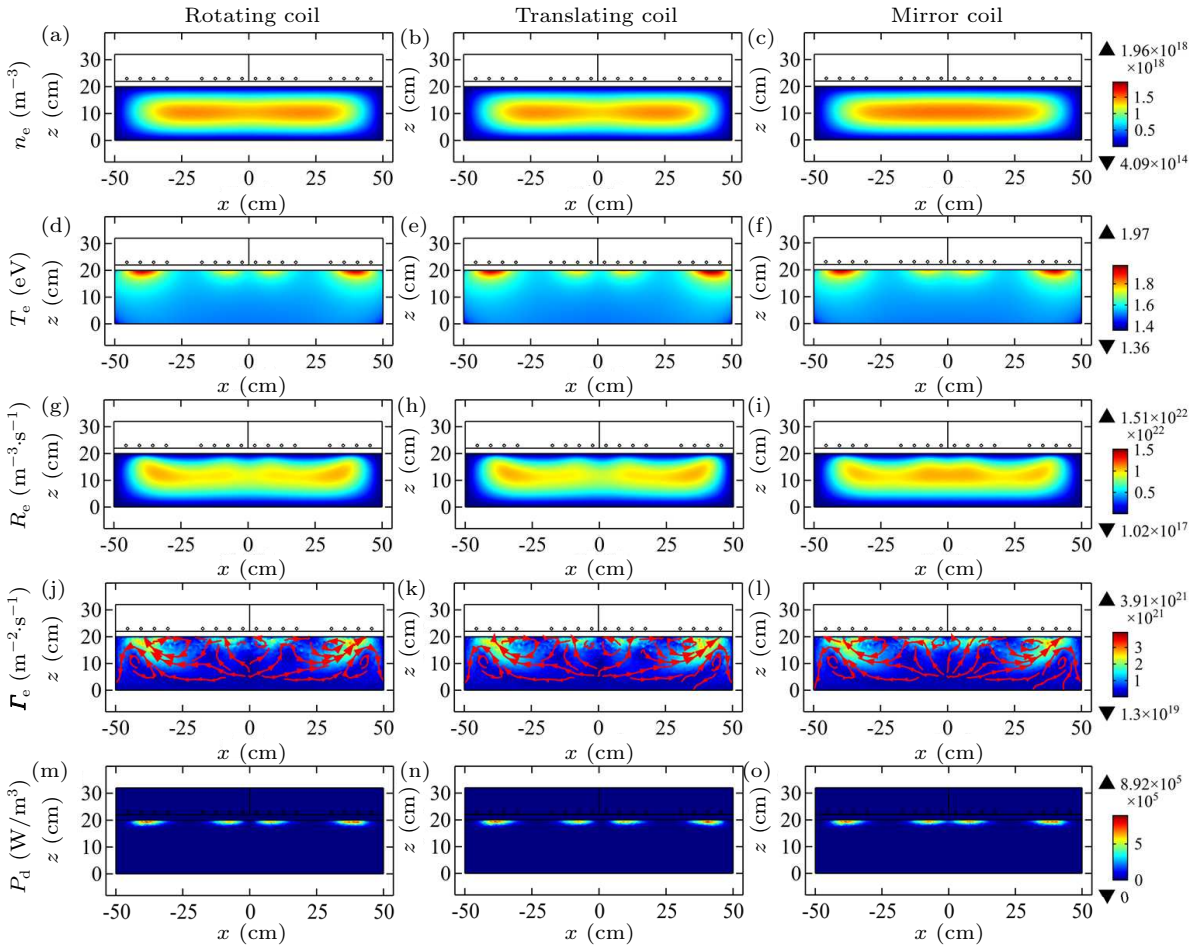


Fig. 14. Distributions of electron density (first row), electron temperature (second row), electron source term (third row), electron flux (fourth row), and deposited power density (fifth row) in the xz-plane ($y = 0$ cm) for different coil structures with electromagnetic shielding.

distribution is largely unaffected by shielding. However, in the mirror coil structure, the electron temperature near $x = 0$ cm evolves from a unimodal to a quasi-bimodal distribution with shielding. This transformation is attributed to the proximity of two peaks in the deposited power density near $x = 0$ cm, as shown in Fig. 14(o).

The spatial heating mechanism in ICP arises because the alternating current in the coil generates a time-varying magnetic field, which induces a vortex electric field. Electrons gain energy from this inductive electric field. After applying electromagnetic shielding to the mirror coil structure, a comparison of Figs. 5(r) and 13(r) shows that the electric field distribution near $x = 0$ cm changes from a centrally concentrated profile to a separated but not completely isolated pattern. Consequently, the two peaks of the deposited power density move closer together; they do not fully merge, ultimately producing the observed quasi-bimodal electron temperature distribution.

3.3. Analysis of plasma uniformity in the *x*-direction

This subsection investigates in detail the influence of coil structure and electromagnetic shielding on plasma uniformity. Figure 15 shows the normalized electron density along the x-direction ($y = 0$ cm, $z = 2$ cm) for various coil structures, with and without electromagnetic shielding. The non-uniformity degree for each configuration is summarized in Table 2. The degree of plasma non-uniformity is defined as

$$\alpha = \frac{n_{\max} - n_{\min}}{2n_{\text{ave}}}, \tag{22}$$

where $n_{\max}$, $n_{\min}$, and n_{ave} represent the maximum, minimum, and average plasma densities, respectively.[15]

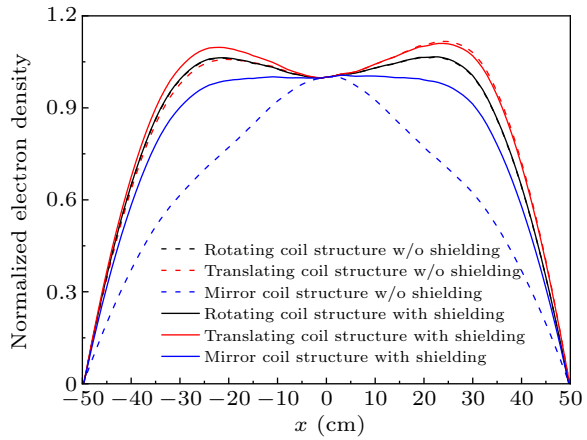


Fig. 15. Normalized electron density distributions along the x-direction ($y = 0$ cm, $z = 2$ cm) for different coil structures, both with and without electromagnetic shielding.

Without electromagnetic shielding, the normalized electron density of the rotating and translating coil structures displays a saddle-shaped profile, while the mirror coil structure exhibits a convex profile. Among the three configurations, the rotating coil structure achieves the best plasma uniformity ($\alpha = 0.065$). The inferior uniformity of the mirror coil structure is due to the strong induced electric field generated by aligned currents near the chamber center, resulting in a high electron source term and centrally concentrated electron density. The translating coil structure shows two distinct peaks in its normalized electron density profile because of its inherent asymmetry, leading to poorer uniformity compared to the rotating coil structure.

With electromagnetic shielding, the rotating and translating coil structures maintain their saddle-shaped profiles. In contrast, the mirror coil structure experiences a notable reduction in central electron density, mitigating overconcentration and promoting a more uniform plasma distribution. This improvement occurs because electromagnetic shielding weakens the mutual inductance between the coils, thereby reducing the central electric field and electron source term. Consequently, the non-uniformity decreases by 18.4%, and the mirror coil structure with electromagnetic shielding achieves the highest plasma uniformity, reaching 94%.

Table 2. Degree of plasma non-uniformity for different coil structures, both with and without electromagnetic shielding.

Coil structure	Non-uniformity degree
Rotating coil — w/o electromagnetic shielding	0.065
Translating coil — w/o electromagnetic shielding	0.087
Mirror coil — w/o electromagnetic shielding	0.244
Rotating coil — with electromagnetic shielding	0.066
Translating coil - with electromagnetic shielding	0.084
Mirror coil - with electromagnetic shielding	0.060

4. Conclusion

In this paper, a 3D fluid model incorporating plasma and electromagnetic field modules was developed to investigate the effects of coil structure and electromagnetic shielding on the spatial distribution and uniformity of plasma in a large-area rectangular RF ICP source (100 cm × 50 cm). The results demonstrate that coil structure significantly influences plasma uniformity. The rotating and translating coil structures produce electron density distributions that are high at off-axis positions and low at the center, whereas the mirror coil structure exhibits a pronounced central peak in electron density. This behavior arises because the spatial distribution of electron density is primarily governed by the electron source term and electron flux. The mirror coil structure generates a stronger central electric field due to the identical current directions in the coils, resulting in higher electron density at the chamber center compared to the rotating and translating coil structures. Furthermore, the electron temperature near $x = 0$ cm exhibits a bimodal distribution for the rotating and translating coil structures, whereas a unimodal distribution is observed for the mirror coil structure. Among the three configurations, the rotating coil structure achieves the best baseline plasma uniformity.

Electromagnetic shielding further enhances plasma uniformity by modulating the spatial distribution of the electromagnetic field. For the rotating and translating coil structures, the electron density distribution — high at off-axis positions and low at the center — remains largely unaffected by shielding. In contrast, incorporating electromagnetic shielding into the mirror coil structure reduces the electron density at the chamber center, promoting a more uniform plasma distribution. Additionally, shielding does not significantly alter the electron temperature distribution in the rotating and translating coil structures. For the mirror coil structure, the electron temperature near $x = 0$ cm decreases with shielding and transitions from a unimodal to a quasi-bimodal distribution. Consequently, the mirror coil structure with electromagnetic shielding achieves a plasma uniformity of 94%, the highest among the studied configurations.

In summary, modifying coil structures and incorporating electromagnetic shielding can markedly improve plasma uniformity in large-area RF ICP sources. Future work will extend the 3D fluid model to array coil structures and include RF bias to further optimize plasma uniformity over large areas. Moreover, experimental and simulation studies involving complex gases (e.g., O_2 and CF_4) will be conducted in conjunction with practical industrial processes.

Acknowledgment

This work was supported by the National Natural Science Foundation of China (Grant Nos. 12075049 and 11935005).

References

[1] Wu Y and Lieberman M A 2000 *Plasma Sources Sci. Technol.* **9** 210
[2] Kim S S, Hamaguchi S, Yoon N S, Chang C S, Lee Y D and Ku S H 2001 *Phys. Plasmas* **8** 1384
[3] Meziani T, Colpo P and Rossi F 2001 *Plasma Sources Sci. Technol.* **10** 276
[4] Lee Y J, Kim K N, Song B K and Yeom G Y 2003 *Thin Solid Films* **435** 275
[5] Jung S J, Kim K N and Yeom G Y 2005 *Surf. Coat. Technol.* **200** 780
[6] Kim K N, Lim J H, Yeom G Y, Lee S H and Lee J K 2006 *Appl. Phys. Lett.* **89** 251501
[7] Kim H J, Hwang H J, Kim D H, Cho J H, Chae H S and Chung C W 2015 *J. Appl. Phys.* **117** 153302
[8] Mehedi H A, Ferrah D, Dubois J, Petit-Etienne C, Okuno H, Bouchiat V, Renault O and Cunge G 2018 *J. Appl. Phys.* **124** 125304
[9] Radovanov S, Samolov A and Distaso D 2019 *Plasma Phys. Control. Fusion* **61** 014031
[10] Zhang T L, Jiang K Y, Liu Z W, Yang L Z, Zhang H B, Ouyang J T and Chen Q 2020 *Plasma Sci. Technol.* **22** 085405
[11] Lee H C, Oh S and Chung C W 2012 *Plasma Sources Sci. Technol.* **21** 035003

[12] Zhao Y, Zhou X H, Gao S R, Song S S and Zhao Y Z 2024 *Plasma Sci. Technol.* **26** 075402
[13] Kim T W, Lee M Y, Hong Y H, Lee M H, Kim J H and Chung C W 2021 *Plasma Sources Sci. Technol.* **30** 025002
[14] Lim J H, Kim K N, Park J K, Lim J T and Yeom G Y 2008 *Appl. Phys. Lett.* **92** 051504
[15] Sun X Y, Zhang Y R, Ye J, Wang Y N and He J X 2021 *Plasma Sci. Technol.* **23** 095404
[16] Son E J, Cho S H and Lee H J 2020 *J. Electr. Eng. Technol.* **15** 2259
[17] Kim K N, Lim J H, Park J K, Lim J T and Yeom G Y 2008 *Jpn. J. Appl. Phys.* **47** 7339
[18] Lee D S, Lee Y K and Chang H Y 2004 *Plasma Sources Sci. Technol.* **13** 701
[19] Lee W H, Cheong H W, Kim J W and Whang K W 2015 *Plasma Sources Sci. Technol.* **24** 065012
[20] O'Connell D, Crintea D L, Gans T and Czarnetzki U 2007 *Plasma Sources Sci. Technol.* **16** 543
[21] Kim K N, Kim M S and Yeom G Y 2006 *Appl. Phys. Lett.* **88** 161503
[22] Huang J W, Zhao M L, Zhang Y R, Gao F and Wang Y N 2023 *Phys. Plasmas* **30** 043508
[23] He Y, Jiang Y L, Jung J, Kim M S, Kim J H and Chung C W 2023 *Plasma Sources Sci. Technol.* **32** 075008
[24] Lee H C, Bang J Y and Chung C W 2011 *Thin Solid Films* **519** 7009
[25] Kim K N, Jung S J and Yeom G Y 2005 *Jpn. J. Appl. Phys.* **44** 8133
[26] 2024 COMSOL Multiphysics Documentation
[27] Kudryavtsev A A and Serditov K Y 2012 *Phys. Plasmas* **19** 073504
[28] Bogaerts A and Gijbels R 1995 *Phys. Rev. A* **52** 3743
[29] Gudmundsson J T, Kouznetsov I G, Patel K K and Lieberman M A 2001 *J. Phys. D: Appl. Phys.* **34** 1100
[30] Kim J H, Kim Y C and Chung C W 2015 *Phys. Plasmas* **22** 073502
[31] Du P C, Zhao M L, Li H, Gao F and Wang Y N 2022 *J. Appl. Phys.* **131** 133301
[32] Xing S Y, Gao F, Zhang Y R, Wang Y J, Lei G J and Wang Y N 2023 *Plasma Sci. Technol.* **25** 105601